Earth-Science Reviews 161 (2016) 224–232

On the origin of the signals observed across the seismic spectrum

J. Díaz

ICTJA-CSIC, c/ Sole Sabaris sn, 08023, Barcelona, Spain

Abstract

The increasing number of broad-band seismic stations recording the full spectrum of the seismic wavefield continuously has boosted interest in background signals recorded in the absence of earthquakes. Different human-made and natural phenomena other than earthquakes result in Earth vibrations that are recorded on seismometers. Those signals have classically been considered as disturbing noise, but in the last decades this view has turned, as it has been shown that seismic data can be used not only to monitor earthquake activity, but also to investigate climatic changes, track hurricanes, monitor river flows, or survey anthropogenic activity, hence making new links between seismology and different research fields. This contribution reviews state-of-the-art knowledge on the sources of seismic energy in different frequency bands using a single, two-weeks-long, seismic data file recorded by a high quality broad-band station located in the Pyrenees. This data allows exploration of the wide spectrum of ground motion, enabling a review of different processes involved in the generation of what seismologists commonly regard as background noise when focusing on ground motion from local and teleseismic earthquakes and explosions recorded in the same time interval.

1 Introduction

Since the early times of the seismic instrumental era it has been clear that seismic instruments were able to record natural and human-made phenomena distinct from earthquakes, including Earth tides, oceanic waves, atmospheric disturbances, or human activity. As an example of this interdisciplinarity, the first recording of a distant earthquake was obtained at Potsdam in April 1889 using an instrument designed by E. von Rebeur-Pashwitz to record Earth tides (Varga, 2009). As early as 1870, Bertelli

(1872) related Earth vibration and atmospheric changes, noting that a pendulum moved continuously for hours or days in periods with disturbed air pressure. The term "microseisms" has been used since the nineteenth century to refer to "the more or less motion of the ground which is not produced by earthquakes or explosions, has periods or pseudo periods of not exceeding several minutes and continuous for many periods" (Gutenberg, 1958). Nowadays, the observation of this background seismic signal has received a new boost with the availability of an increasing number of continuously recording digital broad-band seismic stations and the development of new techniques to use this signal as a tool to retrieve tomographic images of the 3D seismic velocity structure in the crust and uppermost mantle (e.g., Campillo and Paul, 2003). With the present day technology, the seismic spectrum recorded by typical broad-band stations covers about 7 orders of magnitude, extending from 0.01 mHz to hundreds of Hz. Different processes are responsible for the energy recorded in different parts of the seismic spectrum, just as the tessitura of different singers (from soprano to bass) covers the audible spectrum. Overprinting these background signals, earthquakes appear as transient events extending across the spectrum.

Illustrating the different contributions to the seismic signal in a compact way is not easy, as a period of high quality data encompassing phenomena with very different time scales must be identified. We present here data from the vertical component of a Trillium 240 broad-band seismometer installed in the Geodyn facility of the Canfranc underground laboratory (LSC). This site is located in the Central Pyrenees in a former railway tunnel at 350 m beneath the surface and hence benefits from a lower level of seismic noise. Data from this station is sent in near-real time to the Orfeus data center and is openly available from the EIDA nodes (http:/ http://www.orfeus-eu.org/eida/eida.html network code: LC, station code: CANF). We have selected a two-weeks-long period in Fall 2012 gathering the record of Earth tides, microseismic noise, distant and local earthquakes, cultural noise and even less common features, such as the seismic signal generated by water flow in the nearby river (Figure 1). The instrumental response has been removed following standard procedures and the signal referred to ground velocity, expressed in nm/s. A single file encompassing the selected time interval is provided as Supplementary Material.

The vertical seismic trace appears as a smoothly changing amplitude including short, spike-like signals, which correspond to distant and local earthquakes (Figure 1, upper panel). The corresponding spectrogram (Figure 1, lower panel) provides richer information that the time series, as the signal is decomposed to get the time evolution of its frequency content. A color palette, expressed in dB and relative to a reference value of 1 $(m^2/s^4)/Hz$, is used to show the energy distribution. It is easy to observe that, while some frequency ranges remained almost unchanged during the whole investigated period, others show very large variation with time.

Hereafter, we will use this data set to move through the seismic wavefield and discuss the processes involved in signal generation at different frequency ranges.

2 High frequency band

Seismic methods focused in the exploration of the uppermost crustal levels can use man-made signals with frequencies above 50 Hz. Nevertheless, most of the seismic energy propagating significant distances across the Earth has characteristic frequencies not exceeding some tens of Hz. The frequency band between 1 and 50 Hz is generally dominated by human activities (road traffic, machinery etc.) even if other natural sources of noise, such as winds or rainfall, can also contribute, in particular for sites located far from human activity. Analyzing a station located in the New Mexico desert, Withers et al, (1996) found that the seismic background was contaminated by wind-generated noise for winds speed greater than 3 m/s. De Angelis et al. (2012) reported also ground displacements attributed to local atmospheric pressure variations associated with local winds near the Pacific coast of the Olympic Peninsula. Regarding man-made signals, also referred as cultural or anthropogenic noise, it has been shown that it propagates mainly as surface waves, with frequencies higher than 2-4 Hz that attenuate within several kilometers from the source (e.g., Havskov and Alguacil, 2004). Seismic noise investigations, in particular in urban environments, have clearly evidenced the daytime-nightime and working days- weekends variability in the seismic energy at high frequencies (Groos and Ritter, 2009). Riahl and Gestoft (2015) have recently shown that seismic data acquired in dense networks can be used for effective traffic monitoring. Man-made seismic signals have been used for site amplification studies (Bonnefoy-

Claudet, 2006) and even to retrieve velocity-depth profiles of the subsurface depths (Nakata et al., 2011).

Figure 2a shows the seismic trace band-pass filtered between 1 and 10 Hz during four selected days. It can be easily observed that the seismic amplitude is higher in the daytime hours for the 15th, 16th and 17th October, while for Sunday, October 14th, the amplitude level remains low and presents little variation. Such time variation pattern, including large day/night and working/weekend day variations are thus associated to the human activity at the vicinity of the station and, in this particular case, to the traffic intensity in the road tunnel close to the recording site. The daytime seismic trace appears as a non-continuous ensemble of short bursts of relatively large amplitude events, corresponding to the passage of individual vehicles near the station. The spectrogram presented at Figure 2b illustrates the same feature, with working hours having a mean noise level around 5 dB higher.

During days 293-297 (19th-23th October), the spectrogram shows a characteristic pattern in the 1-10 Hz band which clearly overprints the contribution of human-generated noise (Figure 1). This uncommon feature has been investigated by Diaz et al. (2014), and linked to discharge variations of the Aragon River, an Alpine style stream located about 350 m eastward of the recording site. During severe storms, most of the seismic energy recorded at CANF is generated by the impact with the river channel of the bed load particles carried by the stream. The seismic amplitude of the band-passed signal shows large variations which can be correlated with changes in the discharge rate (Figure 2c). The spectrogram (Figure 2d) provides further information, as it shows that the dominant frequency in the 1-2.5 Hz band shifts following the discharge in the Aragon River, while for higher frequencies the energy is distributed more uniformly. Note than at the end of the episode, the dominant frequency smoothly increases, following the progressive descent of the river discharge. Seismic signals generated by river discharges have been identified in a limited number of settings, including Himalayan rivers (Burtin et al., 2008), discharges following the passage of typhoons (Hsu et al., 2011) or large controlled flood experiments (Schmandt et al, 2013). Therefore, under some conditions, seismic data can be used to monitor nearby rivers discharge, hence opening connections between seismology and hydrology.

2 Microseismic band

Since the beginning of seismology it has been known that for stations distributed worldwide, ground motion largely concentrates between 0.04 and 1 Hz, in the so-called microseismic band. In the second half of the XIXth century, some of the fathers of seismology, including Bertelli and Milne, already established a link between meteorology and microseisms (Dewey and Byerly, 1969). As reported by Ebeling (2012), Wiechert (1904) proposed that microseisms were generated by surf breaking at the shoreline and Zoeppritz (1908) related microseisms with moving deep low-pressure systems. Later on, Gilmore (1946) stated that microseisms are associated with cyclones only when those are located far from land.

In the early 1950s, the literature on microseisms was already extensive, as it can be noted in a state-of-the-art report published by Gutenberg (1958), and it was widely accepted that the origin of microseisms is related to oceanic waves, as winds generated by intense cyclonic storm systems over the oceans transfer atmospheric energy into ocean gravity waves that are then partially coupled to the solid Earth, exciting the propagation of seismic waves. The microseismic band has two different peaks related to distinct mechanisms transferring storm-generated gravity waves to the seismic wavefield. The single frequency peak (SF), also referred as the primary microseismic peak, is located around 0.7 Hz, while the double frequency peak (DF), also known as the secondary microseism peak, comprises most of the seismic energy recorded in the absence of large earthquakes and it has a dominant frequency around 0.15 Hz. Longuet-Higgins (1950) established a theory explaining the DF peak as the result of oceanic waves traveling in opposite directions and generating stationary waves that interact to couple energy into elastic waves with a frequency that is twice the ocean wave frequency. Later on, Hasselmann (1963) related the origin of the SF peak to direct pressure fluctuations at the ocean bottom from breaking and/or shoaling waves, generally in shallow waters.

The relationship between ocean waves and seismic background noise has led to the use of the latter for global-scale monitoring of ocean-wave height (Bromirski et al.,1999; Stutzmann et al., 2009; Aster et al., 2010) and to track the time evolution of large hurricanes (Gerstoft et al., 2006; Chen et al., 2015), hence providing a robust link

between seismology and oceanography. Most of the seismic energy generated by ocean waves coupling in the seabed propagates as Rayleigh surface waves and is regularly recorded on land, even at large distances from the coast (Stutzmann et al., 2009), even if recent investigations have also identified a contribution of compressional P-waves (Zhang et al., 2010). The relative importance of coastal and deep ocean sources of DF microseisms is still an open question. Since the 1960's, seismic arrays as LASA, NORSAR, ALPA or Grafenberg have been used to locate the origin of the microseismic signals (Cessaro, 1994; Friedrich et al., 1998). Different authors have described observations and synthetic models favoring a near-coastal origin (Schulte-Pelkum et al., 2004; Gerstoft and Tanimoto, 2007; Traer et al., 2012; Bromirski et al., 2013). However, DF sources located in deep oceans have also been identified (Stehly et al., 2006; Landes et al., 2010; Stutzmann et al., 2012; Obrebski et al., 2012), in some cases related to the passage of moving storms (Chevrot et al., 2007).

Figure 3 presents the seismic signal in the microseismic band and clearly shows that the energy level changes substantially over time. The filtered seismic trace (Figure 3a, lower panel) shows four bursts of increased energy centered on days 287, 289, 292 and 295, the latter two being the most energetic. In order to relate those episodes with ocean wave activity, Figure 3b shows daily snapshots of the significant wave-height hindcast for the central Atlantic. As it can be observed, the first two intervals correlate with the occurrence of storms near the southern coast of Greenland, a region prone to generate microseismic noise. The large signal centered on day 292 correlates with the arrival of high oceanic waves at the Bay of Biscay coast, and with the passage of hurricane Sandy along of North-America coast. The last episode, centered on day 295, is dominated by large waves in the deep waters south of Iceland (Figure 3b). The inspection of the corresponding spectrogram (Figure 3, upper panel) provides richer information on the separate contributions of SF and DF peaks. The SF band, delineated by a dashed box, follows the time variation observed in the seismic trace. The lower part of the DF, in the 0.1-0.2 Hz range, shows a similar pattern, in particular for the 291-293 and 294-297 episodes, while energy variations at higher frequencies have a different pattern. Bromirski et al., (2005) have proposed a division of the DF peak into two zones on the basis of data from the ocean bottom seismometer H2O. Frequencies beneath 0.2 Hz will be excited at coastal regions, while higher frequency energy will be generated in open waters. This interpretation seems consistent with our observations, as high energy

intervals are observed simultaneously in the SF and lower DF peaks but not in the higher DF zone.

During the episode encompassing days 294-297 of year 2012, the SF and the lower part of the DF peaks show dispersion, with the dominant frequency smoothly increasing over time. Bromirski et al. (2013) observed a similar dispersion for stations located near the western US coast and proposed that dispersion shows how the oceanic depression approaches the coastline. The dispersion observed in our data for the SF and lower DF peaks between days 294 and 295 reflects the progressive arrival of high waves generated by the cyclone, which moves north to south along the central Atlantic, up to the coast of the Bay of Biscay. The most energetic time interval in the upper part of the DF peak corresponds to days 295-296 and correlates with the occurrence of high waves above the deep waters of the central Atlantic, hence arguing in favor of a source region located at open waters for this zone of the spectrum. The 291-292 episode has large energy level in both SF and DF, but no dispersion is observed, suggesting that the location of signal-generating storm remains stable, or that the source region is far from the European coasts. For this episode the energy increase in the upper DF peaks is lower than in the previous case and starts nearly one day later than in the SF and lower DF bands, suggesting that it can be a multiple sources episode, including the arrival of high waves in the Bay of Biscay area and the passage of the hurricane Sandy near the coast of North America (Chen et al., 2015; Sufri et al., 2014).

3 Earth's hum

Moving to lower frequencies, the frequency band ranging between 2 and 20 mHz (periods of 300-30s) is usually referred as "Earth's hum" and is observed worldwide at high quality sites. Following large earthquakes, the normal modes of the Earth are excited, resulting in energy peaks extending from 0.3 mHz (54 minutes) to 10 mHz and presenting maximum energy in the 2-8 mHz range. Normal modes were first observed unambiguously by Benioff et al (1961) following the great Chile earthquake in 1960. Since then, normal modes have played a key role in deriving the radial variations of density, P-wave and S-wave velocities for the whole Earth (Gilbert and Dziewonski,

1975), in calculating synthetic seismograms (Harvey, 1981) and in evaluating centroid moment tensors of large earthquakes (Dziewonski et al., 1981).

Nawa et al. (1998), using data from a superconducting gravimeter in East Antarctica, first showed that the normal modes can be excited in the absence of earthquakes, though the effect is subtle. The direct coupling of atmospheric pressure variations has been proposed as the mechanism responsible of the excitation of these modes (Sorrells, 1971; Suda et al., 1998). However, most recent investigations tend to neglect the effect of pressure changes, favoring an origin related to the so-called infragravity waves (Tanimoto, 2005; Ardhuin et al., 2015). Infragravity waves (IG) are small amplitude oceanic surface waves with periods exceeding 25s (Webb, 2007). They are generated by nonlinear interactions of wind-driven waves close to shorelines and propagate then in the open ocean, where they are ubiquitous, generating pressure fluctuations which couple to vertical movements of the solid Earth that can be recorded inland. Rhie and Romanowicz, (2004) showed that Earth's hum is mainly generated in the northern and southern oceans during their respective winter seasons by the interaction of IG waves and seafloor topography. Although hum can be excited by IG waves in the deep ocean (Webb, 2008), the dominant hum generation seems to be coastal (Bromirski and Gerstoft, 2009; Ardhuin et al., 2015). Traer and Gerstoft (2014) proposed that microseisms and hum have a common origin related to the different interaction of first-order pressure waves generated by oceanic waves; DF will be produced by sum interactions while the Earth's hum will be produced by difference interactions.

Figure 3c shows the filtered seismic trace and the corresponding spectrogram in the Earth's hum band. The increased energy observed during days 286 and 298 is not related to Earth's hum, but to the global cycling waves and normal modes generated by a magnitude 6.7 seismic event with epicenter near the south coast of Papua, Indonesia (see section 5) and a magnitude 6.5 event in Costa Rica. The episode with maximum energy in this band is observed between days 291-294, a time interval also showing increased energy in the microseismic peak. As already pointed out in the previous section, during days 291-294 hurricane Sandy was moving along the coast of North America, allowing its seismic detection (Chen et al., 2015; Sufri et al., 2014). Following Rhie and Romanowicz (2006), we propose that seismic energy in the Earth's hum band

can be attributed to IG waves generated by hurricane Sandy near the coast of North America, which radiated free energy travelling through the ocean and coupled to the seafloor near the European coast. For the rest of the investigated period, there is low correlation between energy variations in the microseismic and Earth's hum bands.

4 Solid Earth tides

The gravitational effects of the Moon and the Sun, responsible of the tides in ocean waters, also affect the solid earth, leading to displacements which can reach up to 30 cm. The solid Earth tides have characteristic periods around 12 and 24 hours (0.0231 and 0.0115 mHz respectively) and cover the lowermost part of the seismic spectrum.
Earth tides can be used to get information of the Earth interior, as estimations of the flattening of the core-mantle boundary, or to improve the accuracy of other measurements, as the positions given by GNSS networks (Agnew, 2007). Earth tides are typically recorded using tiltmeters, strainmeters, gravimeters or space geodesy instruments (Agnew, 1986), but the displacements induced by solid Earth tides produce tilting that can also be detected by broad-band seismic sensors, in some cases with accuracy similar to supercomputing gravimeters (Pillet et al.,1994; Freybourger et al., 1997). However, using broad-band seismometers to monitor Earth tide variations is only possible in locations with favorable conditions, as these signals are often masked by the effect of temperature and pressure changes, which can deform the vault or sensor casing, modifying the instrument response or altering the mechanical properties of the material surrounding the sensor, hence producing a signal not related to the elastic deformation of the Earth (Wolin et al., 2015).

To observe the record of Earth tides in our data, we use the raw, uncorrected signal, as the mathematical operations involved in the removal procedure of the instrument response present numerical instabilities when dealing with such low frequencies. Figure 4a shows the raw data downsampled to one sample per minute. This procedure acts as a low-pass filter, enhancing the long term variations in the signal. Note that the amplitude peaks observed in the seismic trace (October 12th, 20th, 23th and 24th) correspond to the arrival of surface waves from catalogued earthquakes. The theoretical Earth tide,

304 calculated using the Ertid program of the spotl package (Agnew, 2002) and expressed as
305 potential heights is included at Figure 4a to compare with the seismic data.
306
307 The downsampled seismic trace and the theoretical solid Earth tide appear to have a
308 very good correlation. During the first days, the semi-diurnal component of tide
309 dominates the signal in both the seismic and theoretical data. After 4/5 days, the
310 theoretical Earth tide is progressively dominated by the diurnal component. The seismic
311 trace also shows this tendency, even if the semi-diurnal component retains more energy.
312 This probably reflects the fact that other sources, such as tilting due to temperature or
313 pressure variations, are also contributing to the seismic signal. During the final four
314 days, the amplitude of both signals diminishes as an effect of the fortnightly component
315 of tides. Figure 4b shows the spectrum of the seismic trace after applying a FFT to the
316 full dataset. As expected, the most prominent peak corresponds to the semi-diurnal M2
317 component of tide, with a period of 12.241 h (2.24 10^{-5} Hz) while the second peak is
318 close to the K1 and O1 diurnal tidal constituents, with periods of 23.934 and 25.818
319 hours respectively (1.16 10-6 / 1.07 10^{-5} Hz). Therefore, Earth tides are the dominant
320 source of signal in this very low frequency range.
321
322
323 **5 Seismic events**
324
325 The identification of different seismic phases following the occurrence of earthquakes
326 and recorded at specific distances has been the major tool to understand the internal
327 structure of the Earth, including its classical division into crust, mantle and outer and
328 inner cores. To complete the description of the seismic wavefield in Figure 5, we
329 present a couple of examples of nearby and distant earthquake recordings, hence
330 allowing its comparison with the seismic signals discussed previously. A detailed
331 analysis of the different phases identified in each event is out of the scope of this
332 contribution and for more details the reader is referred to the large bibliography
333 available on that point (e.g. Bormann et al., 2014; Kulhanek and Persson, 2011). It is
334 worthy to note that other classes of seismic events do exist, including the tremors and
335 short duration events associated to volcano activity (e.g. Chouet, 1996) or the non-
336 volcanic tremors and low frequency earthquakes associated to subduction zones (Shelly
337 et al., 2007). Additionally, seismometers can record other natural phenomena, from

shock waves generated by meteorites (Edwards et al., 2008) to ground motion resulting from snow avalanches or landslides (e.g. Suriñach et al., 2005).

The seismic events appear in the spectrogram as narrow lines crossing a large part of the spectrum, extending across at least three orders of magnitude of frequency. The distant (teleseismic) event is a Mw 6.7 earthquake with epicenter near the south coast of Papua (Indonesia), at a distance close to 14000 km from the recording site. The differences in velocity between compressional, shear, and surface waves, as well as the different ray paths followed by each phase, result in several hours of shaking associated with this event. Figure 5a presents 3 hours of data, but smaller-amplitude signals, including global circling waves, can be identified at even later times. The signal of this event overprints the background seismic noise and can be identified even within the band normally associated with the microseismic peak. The spectrogram shows that this teleseismic event is recorded from at least 3 mHz to 2 Hz, even if most of the energy concentrates between 0.03 and 0.08 Hz, corresponding to the arrival of the surface waves train. The presence of energy bursts in this frequency range is in fact an useful approach to identify the arrival of teleseismic signals in the raw seismic data. The USGS catalogue reports 20 earthquakes with magnitude larger that 5.5 during the investigated period, most of which can be identified at Figure 1 by the presence of reddish colors around 0.06 Hz.

Figure 5b shows the arrival of a local event with local magnitude 3.8 and epicenter near the town of Lourdes, at a distance of roughly 60 km from the recording site (Renass, http:// http://renass.unistra.fr/evenements/517a51d8136522dc7e7fe116). Note that the time scale is now very different from the previous case, with a total duration of about 40 s, which is about 100 times shorter than for the distant event. The frequency content is also very different, as the energy associated to this event can be identified between 0.8 to 20 Hz in our spectrogram and extends to higher frequencies in the original data. The Renass catalogue report two additional events with magnitude above 2.0 on dates 15/10/2012 20:08 and 16/10/2016 01:51. The arrival of those events can be identified at Figure 1 as light blue lines, but having amplitude similar to anthropogenic noise and hence making them difficult to recognize in a simple inspection of the spectrogram.

6 Conclusions

Recordings of ground motion (seismograms) include much more information than the transient signals associated with earthquakes. Although this fact has been known since the early times of instrumental seismology, the availability of large amounts of waveform data from continuously recording broad-band stations allow nowadays a better understanding of the different natural and man-made processes dominating the generation of the background signal in the different frequency bands of the seismic spectrum. Nevertheless, disseminating this information is not easy, as examples of very different processes, with characteristic periods spanning from a few seconds to several hours, have to be collected in the seismic data.

The excellent quality of the CANF broad-band seismic station recordings has allowed to select a two-week long period of ground motion shaking containing the effects of a wide variety of natural and artificial phenomena. The spectrogram shown at Figure 1 allows to identify in a single image seismic signals with frequencies ranging from 3 mHz to 20 Hz. Additional identification of the Earth tide signature results in a seismic dataset extending over six orders of magnitude in frequency and resulting from very different processes, from cars moving in the vicinity of the recording site to the passage of the Sandy hurricane along the North America coast or to the deformation induced by the gravitational effects of the Moon and the Sun. The present-day knowledge on how those processes generate seismic signals is reviewed and relevant references are provided to the reader for further information. The final conclusion can be that, also in the seismological world, “one person’s noise is another person’s signal”.

Acknowledgments

I want to acknowledge all the staff of the Laboratorio Subterraneo de Canfranc (LSC) for their help in the installation and maintenance of the Geodyn facility. This is a contribution of the Geodyn project [MICINN ICTS2009-33]. Additional funding is provided by the Red TopoIberia-Iberarray CGL2014-54582-REDC], the MISTERIOS project [CGL2013-48601-C2-1-R] and the Generalitat de Catalunya grant 2009SGR1595. Many of the figures were produced using the Generic Mapping Tools (GMT) software

405 (Wessel et al., 2013). Finally, I want also to acknowledge Paul Richards and an
406 anonymous reviewer for their helpful comments.
407
408

References

Agnew, DC. 1986. Strainmeters and Tiltmeters. Reviews of Geophysics. 24:579-624.

Agnew, DC. 2007. Earth Tides. Treatise on Geophysics and Geodesy. (Herring TA, Ed.).:163-195., New York: Elsevier

Agnew, D. C. (2012). *SPOTL: Some Programs for Ocean-Tide Loading*, SIO Technical Report, Scripps Institution of Oceanography, Web Access

Ardhuin, F., Gualteri, L. and Stutzmann, E., (2015). How ocean waves rock the Earth: Two mechanisms explain microseisms with periods 3 to 300 s., Geophys. Res. Lett., 42: 765–772. doi:10.1002/2014GL062782

Aster, R.C., McNamara, D. E. and Peter D. Bromirski, P.D., (2010). Global trends in extremal microseism intensity, Geophys. Res. Lett., 37, L14303, doi:10.1029/2010GL043472, 2010

Benioff, H., Press, F. and Smith, S. (1961). Excitation of the free oscillations of the Earth by earthquakes. J. Geophys. Res. 66, 2, 605-619

Bertelli, T. (1872). Osservazoni sui piccoli movimenti dei pendoli in relazione ad alucuni fenomeni meteorologiche, Boll. Meteorol. Osserv. Coll. Roma 9, 10 pp.

Bonnefoy-Claudet, S., F. Cotton, and P.-Y. Bard (2006), The nature of noise wavefield and its applications for site effects studies: A literature review, Earth Sci. Rev., 79, 205–227.

Bormann, P., Klinge, K., Wendt, S. (2014): Data Analysis and Seismogram Interpretation. - In: Bormann, P. (Ed.), *New Manual of Seismological Observatory Practice 2 (NMSOP-2)*, Potsdam : Deutsches GeoForschungsZentrum GFZ, pp. 1—126. DOI: http://doi.org/10.2312/GFZ.NMSOP-2_ch11

442 Bromirski, P.D. and Gerstoft, P., 2009. Dominant source regions of the Earth's hum are
443 coastal, Geophys. Res. Lett., 36. 1–5.
444
445 Bromirski, P. D., Flick, R.E., and Graham, N., (1999). Ocean wave height determined
446 from inland seismometer data: Implications for investigating wave climate changes in
447 the NE Pacific, J. Geophys. Res. - C, 104, 20,753–20,766.
448
449 Bromirski, P. D., Duennebier, F.K., and Stephen, R.A., (2005). Mid-ocean microseisms,
450 Geochem. Geophys. Geosyst., 6, Q04009, doi:10.1029/2004GC000768.
451
452 Bromirski, P. D., Stephen, R.A., and Gerstoft, P., (2013). Are deep-ocean-generated
453 surface-wave microseisms observed on land?, J. Geophys. Res. Solid Earth, 118, 3610–
454 3629, doi:10.1002/jgrb.50268
455
456 Burtin, A., L. Bollinger, J. Vergne, R. Cattin, and J. L. Nabelek (2008). Spectral
457 analysis of seismic noise induced by rivers: A new tool to monitor spatiotemporal
458 changes in stream hydrodynamics, J. Geophys. Res., 113, B05301,
459 doi:10.1029/2007JB005034.
460
461 Cessaro, R. K. (1994), Sources of primary and secondary microseisms, Bull. Seismol.
462 Soc. Am., 84, 142–148.
463
464 Chen, X., Tian, D., and Wen, L., (2015). Microseismic sources during Hurricane Sandy.
465 J. Geophys. Res. Solid Earth, 120, 6386–6403, doi:10.1002/2015JB012282.
466
467 Chevrot, S., Sylvander, M., Ponsolles, C., Benahmed, S., Lefevre, J.M. and Paradis, D.,
468 (2007). Source locations of secondary microseisms in western europe: evidence for both
469 coastal and pelagic sources, J. Geophys. Res., 112, B11301,
470 doi:10.1029/2007JB005059.
471
472 Campillo, M., and Paul, A. (2003). Long range correlations in the diffuse seismic
473 coda. Science, 299, 547-549
474
475 Chouet, 1996

476 Chouet, B.H., (1996). Long-period volcano seismicity: its source and use in eruption
477 forecasting. Nature, 380, 309–316
478
479 De Angelis, S. And Bodin, P., (2012). Watching the Wind: Seismic Data Contamination
480 at Long Periods due to Atmospheric Pressure-Field-Induced Tilting, Bull. Seismol. Soc.
481 Am, 102, 3, 1255–1265, doi: 10.1785/0120110186
482
483 Dewey, J. and Byerly, P., (1969). The early history of seismometry (to 1900). Bull.
484 Seismol. Soc. Am., 59, 183-227.
485
486 Díaz, J., Ruíz, M., Crescentini, L., Amoruso, A., and Gallart , J. (2014). Seismic
487 monitoring of an Alpine mountain river, J. Geophys. Res. Solid Earth, 119, 3276–3289,
488 doi:10.1002/2014JB010955.
489
490 Dziewonski, A.M., Chou, T.-A. and Woodhose, J.H. (1981). Determination of
491 earthquake source parameters from waveform data for studies of global and regional
492 seismicity, J. Geophys. Res., 86, B4, 2825-2852
493
494 Edwards, W.N., Eaton, D.W. and Brown, P.G. (2008) Seismic observations of meteors:
495 coupling theory and observations, Rev. Geophys., 46, RG4007,
496 doi:10.1029/2007RG000253
497
498 Ebeling, C.W., (2012). Inferring ocean storm characteristics from ambient seismic
499 noise, Advances in Geophysics, 53, 133.
500
501 Freybourger, M., Hinderer, J. and Trampert, J. (1997). Comparative study of
502 supercomducting gravimeters ans broadband seismometers STS-1/Z in seismic and
503 subseismic frequency bands. Phys. Earth Planet. Int., 101, 203-217.
504
505 Friedrich A., Krüger F., Klinge K. Ocean-generated microseismic noise located with the
506 Gräfenberg array. J. Seismol. 1998;2(1):47-64.
507
508 Gerstoft, P., Fehler, M.C. and Sabra, K. G. (2006). When Katrina hit California.
509 Geophys. Res. Lett., 33, L17308, doi:10.1029/2006GL027270

Gilmore, M.H., (1946). Microseisms and ocean storms, Bull. Seismol. Soc. Am., 36, 89-119.

Groos, J. C., and J. R. R. Ritter (2009), Time domain classification and quantification of seismic noise in an urban environment, *Geophys. J. Int.*, *179*(2), 1213–1231, doi:10.1111/j.1365-246X.2009.04343.x.

Gutenberg, B., (1958). Microseism. Advances in Geophysics, 5, 53-92.

Harvey, D.J. (1981). Seismogram synthesis using normal mode superposition: the locked mode approximation Geophys. J. Int. (1981) 66 (1): 37-69 doi:10.1111/j.1365-246X.1981.tb05947.x

Hasselmann, K. (1963). A statistical analysis of the generation of microseisms, Rev. Geophys., 1, 177–210.

Havskov, J., and G. Alguacil (2004). Instrumentation in Earthquake Seismology, in Modern Approaches in Geophysics Series, Vol. 22, Springer, Dordrecht, The Netherlands, 328 pp.

Hsu, L., N. J. Finnegan, and E. E. Brodsky (2011), A seismic signature of river bedload transport during storm events, Geophys. Res. Lett., 38, L13407, doi:10.1029/2011GL047759.

Kulhanek, O., & Persson, L. (2011). Seismogram Interpretation. In Encyclopedia of Solid Earth Geophysics (pp. 1315-1324). Springer Netherlands.

Landes, M., Hubans, F., Shapiro, N.M., Paul, A., and Campillo, M., (2010). Origin of deep ocean microseims by using teleseismic body waves, J. Geophys. Res., doi:10.1029/2009JB006918.

Longuet-Higgins, M. S. (1950). A theory of the origin of microseisms, Philos. Trans. R. Soc. London, Ser. A, 243(857), 1–35, doi:10.1098/rsta.1950.0012.

Lorenzo, J.M., (2010). Seismology in sport. Seism. Res. Lett., 81, 3, 526-529.

Nakata, N., R. Snieder, T. Tsuji, K. Larner, and T. Matsuoka (2011), Shear wave imaging from traffic noise using seismic interferometry by cross-coherence, Geophysics, *76*(6), SA97–SA106, doi:10.1190/geo2010-0188.1

Nawa, K., Suda, N., Fukao, Y., Sato, T., Aoyama, Y. and Shibuya, K., (1998). Incessant excitation of the Earth's free oscillations. Earth Planets Space*,* 50**,** 3–8.

Nishida, K., Kobayashi, N. and Fukao, Y., (2000). Resonant oscillations between the solid Earth and the atmosphere, Science*,* 287**,** 2244–2246.

Obrebski, M. J., Ardhuin, F., Stutzmann, E., and Schimmel, M. (2012). How moderate sea states can generate loud seismic noise in the deep ocean, Geophys. Res. Lett., 39, L11601, doi:10.1029/2012GL051896

Pillet, R., Florsch, N., Hinderer, J. and Rouland, D. (1994). Performance of Wielandt-Streckeisen STS-1 seismometers in the tidal domain-preliminary results. Phys. Earth Planet. Int., 84, 161-178.

Rhie, J., and Romanowicz, B., (2004). Excitation of Earth's continuous free oscillations by atmosphere–ocean–seafloor coupling, Nature, 431(7008), 552–556, doi:10.1038/nature02942.

Rhie, J. and Romanowicz, B., (2006). A study of the relation between ocean storms and the Earth's hum, Geochem. Geophys. Geosyst., 7, Q10004, doi:10.1029/2006GC001274.

Riahi, N., and P. Gerstoft (2015). The seismic traffic footprint: Tracking trains, aircraft, and cars seismically, Geophys. Res. Lett., *42*, 2674–2681, doi:10.1002/2015GL063558.

Schmandt, B., Aster, R.C., Scherler, D., Tsai, V.C. and Karlstrom, K. (2013). Multiple fluvial processes detected by riverside seismic and infrasound monitoring of a

577 controlled flood in the Grand Canyon. Geophys., Res. Let., 40, 4858–4863,
578 doi:10.1002/grl.50953.
579
580 Schulte-Pelkum, V., Earle, P.S., and Vernon, F.L., (2004), Strong directivity of ocean-
581 generated seismic noise, Geochem. Geophys. Geosyst., 5, Q03004,
582 doi:10.1029/2003GC000520.
583
584 Shelly, D.R., Beroza, G.C. and Ide, S., (2007). Non-volcanic tremor and low-frequency
585 earthquake swarms. Nature, 446, 305-307.
586
587 Sorrells, G. G. (1971). A preliminary investigation into the relationship between long-
588 period seismic noise and local fluctuations in the atmospheric pressure field, Geophys.
589 J. Roy. Astron. Soc. 26, no. 1-4, 71–82, doi 10.1111/j.1365-246X.1971.tb03383.x.
590
591 Stutzmann, E., Schimmel, M., Patau, G. and Maggi, A., (2009). Global climate imprint
592 on seismic noise, Geochem. Geophys. Geosyst., 10, Q11004,
593 doi:10.1029/2009GC002619.
594
595 Suriñach, E., I. Vilajosana, G. Khazaradze, B. Biescas, G. Furdada, and J. M. Vilaplana
596 (2005), Seismic detection and characterization of landslides and other mass movements,
597 Nat. Hazards Earth Syst. Sci., 5 (6), 791–798, doi:10.5194/nhess-5-791-2005.
598
599 Stutzmann, E., Ardhuin, F., Schimmel, M., Mangeney, A., and Tatau, G., (2012),
600 Modelling long-term seismic noise in various environments, Geophys. J. Int.,
601 doi:10.1111/j.1365-246X.2012.05638.x.
602
603 Suda, N., Nawa, K. and Fukao, Y., (1998). Earth's background free oscillations,
604 Science, 279, 2089–2091.
605
606 Sufri, O., Kopera, K.D., Burlacu, R. and de Foy, B. (2014). Microseisms from
607 Superstorm Sandy. Earth and Planetary Science Letters 402 (2014) 324–336,
608 doi:10.1016/j.epsl.2013.10.015
609

610 Tanimoto, T. (2005), The oceanic excitation hypothesis for the continuous oscillations
611 of the Earth, Geophys. J. Int., 160, 276– 288, doi:10.1111/j.1363-246X.2004.02484.x.
612
613 Traer, J. and Gerstoft, P., (2014). A unified theory of microseisms and hum, J.Geophys.
614 Res., 119, 3317–3339.
615
616 Traer, J., Gerstoft, P., Bromirski, P.D. and Shearer, P.M., (2012). Microseisms and hum
617 from ocean surface gravity waves, J. Geophys. Res., 117, B11307,
618 doi:10.1029/2012JB009550.
619
620 Varga, P. (2009). Common roots of modern seismology and of earth tide research. A
621 historical overview. J. Geodynamics, 48, 241-246, doi: 10.1016/j.jog.2009.09.032
622
623 Webb, S.C., (2007). The Earth's 'hum' is driven by ocean waves over the continental
624 shelves, Nature, 445. 754–756.
625
626 Webb, S.C., (2008). The Earth's hum: the excitation of Earth normal modes by ocean
627 waves, Geophys. J. Int., 174, 542–566.
628
629 Wessel, P., W. H. F. Smith, R. Scharroo, J. F. Luis, and F. Wobbe, (2013) Generic
630 Mapping Tools: Improved version released, EOS Trans. AGU, 94, 409-410.
631
632 Wiechert, E., (1904). Verhandlungen der Zweiten Internationalen Seismologischen
633 Konferenz, Gerl. Beitr. Geophys. Ergan- zungsbd. 2, 41-43.
634
635 Withers, M., Aster, R., Young, C., and Chael, E., (1996). High-frequency analysis of
636 seismic background noise and signal-to-noise ratio near Datil, New Mexico, Bull.
637 Seismol. Soc. Am., 86, 1507–1515.
638
639 Wolin, E., van der Lee, S., Bollmann, T.A., Wiens, D. A., Revenaugh, J., Darbyshire,
640 F.A., Frederiksen, A.W., Stein, S. and Wysession, M. E., (2015). Seasonal and Diurnal
641 Variations in Long-Period Noise at SPREE Stations: The Influence of Soil
642 Characteristics on Shallow Stations' Performance. Bull. Seismol. Soc. Am.,
643 doi:10.1785/0120150046

644

645 Zhang, J., Gerstoft, P., and Bromirski, P.D., (2010). Pelagic and coastal sources of P-
646 wave microseisms: Generation under tropical cyclones, Geophys. Res. Lett., 37,
647 L15301, doi:10.1029/2010GL044288.

648

649 Zoeppritz, K., (1908). Seismische registrienrungen in Göttingen im jahne 1906,
650 Nachrichten von der Königlischen Gesellschaft der Wissenschaften zu Göttingen.
651 Mathematisch-Physilische Klasse, 129-200.

652

653 **Figure Captions**

654

655 **Figure 1**: Upper panel: Vertical component of the unfiltered seismic signal after
656 removal of the instrument response. The vertical scale is expressed in nm/s. Lower
657 panel: Spectrogram of the above signal between 0.03 and 20 Hz, computed using
658 overlapping 1-hour long windows. The color scale represents the power spectral density
659 (PSD) expressed in dB relative to 1 (m^2/s^2)/Hz, with the reddish colors representing
660 large energy values. Time scale is shown as dates and Julian days.

661

662 **Figure 2**: a) Seismic trace filtered between 2 and 10 Hz, showing the day/night
663 variation of the anthropogenic seismic signals. b) Corresponding spectrogram. Note that
664 the color palette is different from Figure 1 to enhance the visibility of the day/night
665 variations. c) Vertical component filtered between 1 and 10 Hz to image the seismic
666 signal generated by the Aragon River discharge after a large rainfall episode,
667 represented by a red line. d) Corresponding spectrogram. The insets indicate the
668 intervals in the complete spectrogram that have been analyzed.

669

670 **Figure 3**: a) Upper panel: Spectrogram of the frequency range including the
671 microseimic peak. The blue and grey dashed boxes outline respectively the primary and
672 secondary peaks. Lower Panel: Seismogram filtered between 0.04 and 0.8 Hz. b)
673 Significant wave heights from the NOAA Wavewatch III hindcast model
674 (http://polar.ncep.noaa.gov/waves/download.shtml?). Each frame represents the
675 snapshot at 12:00 of the corresponding day. c) Upper panel: Spectrogram for the Earth's
676 hum frequency range. Lower Panel: Seismic trace band pass filtered between 3 and 30
677 mHz. The insets allow to locate the analyzed intervals in the complete spectrogram.

678

679 **Figure 4**: a) Theoretical solid Earth tide, represented as potential height (red dashed
680 line) and raw vertical seismic trace downloaded to 1 sample per minute (black line). The
681 correlation between both signals is clear for the semi-diurnal, diurnal and fortnightly
682 components of tide. b) Spectrum of the seismic trace. The two peaks correspond to the
683 frequencies of the main diurnal and semi-diurnal components of tide, shown by arrows.

684

685 **Figure 5**: a) Spectrogram and seismic trace during the arrival of the seismic waves from
686 a distant Mw 6.7 event with epicenter near the south coast of Papua, Indonesia (approx.

distance: 14000 km) b) Spectrogram and seismic trace during the arrival of the seismic waves from a local event with magnitude 3.8 Mlv and epicenter near the town of Lourdes, approximately 60 km away from the recording site. The black arrows in the inset allows to locate both events.

Supplementary Material

CANF_Z_Corrected_signal.sac

SAC file including the vertical seismic component of the CANF station between 2012-10-11 00:00 and 2012-10-25 00:00, after removal of the instrument response and sampled at 50 samples per second.

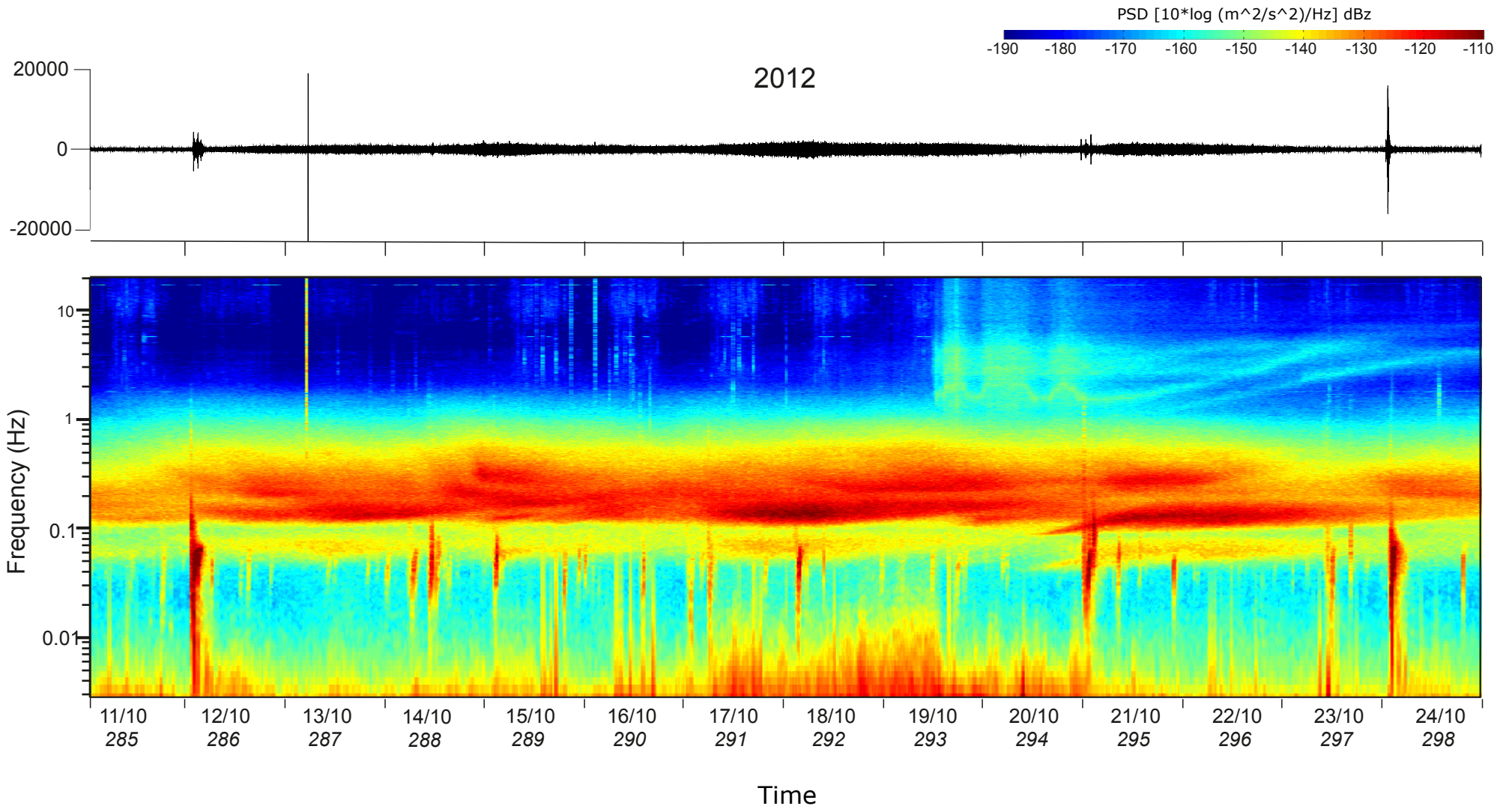

Figure 1: Upper panel: Vertical component of the unfiltered seismic signal after removal of the instrument response. The vertical scale is expressed in nm/s. Lower panel: Spectrogram of the above signal between 0.003 and 20 Hz, computed using overlapping 1-hour long windows. The color scale represents the power spectral density (PSD) expressed in dB relative to 1 (m2/s2)/Hz, with the reddish colors representing large energy values. Time scale is shown as dates and Julian days.

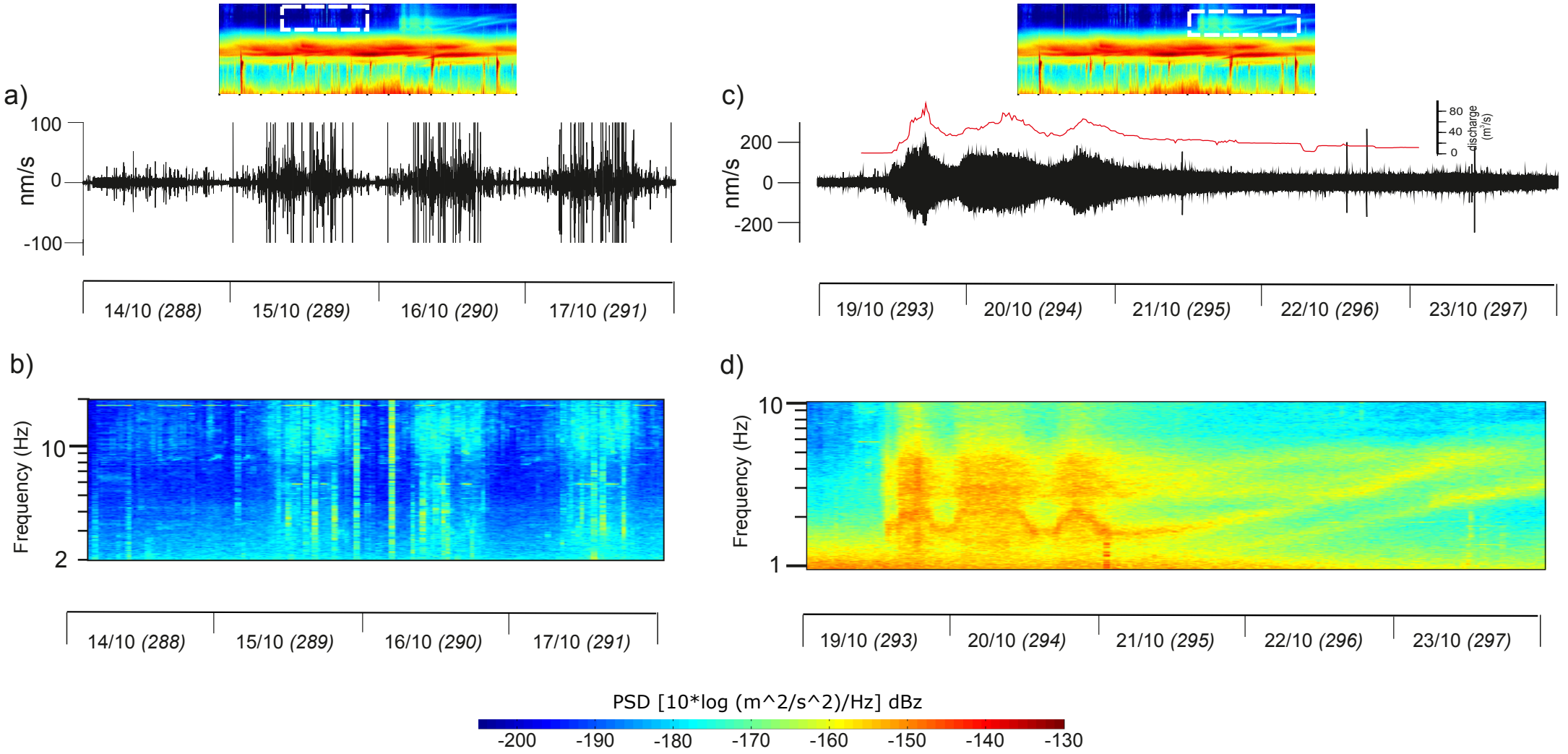

Figure 2: a) Seismic trace filtered between 2 and 10 Hz, showing the day/night variation of anthropogenic seismic signals. b) Corresponding spectrogram. c) Vertical component filtered between 1 and 10 Hz to image the signal generated by the Aragon River discharge after a significant rainfall episode, represented by a red line. d) Corresponding spectrogram. The insets indicate the intervals in the complete spectrogram that have been analyzed.

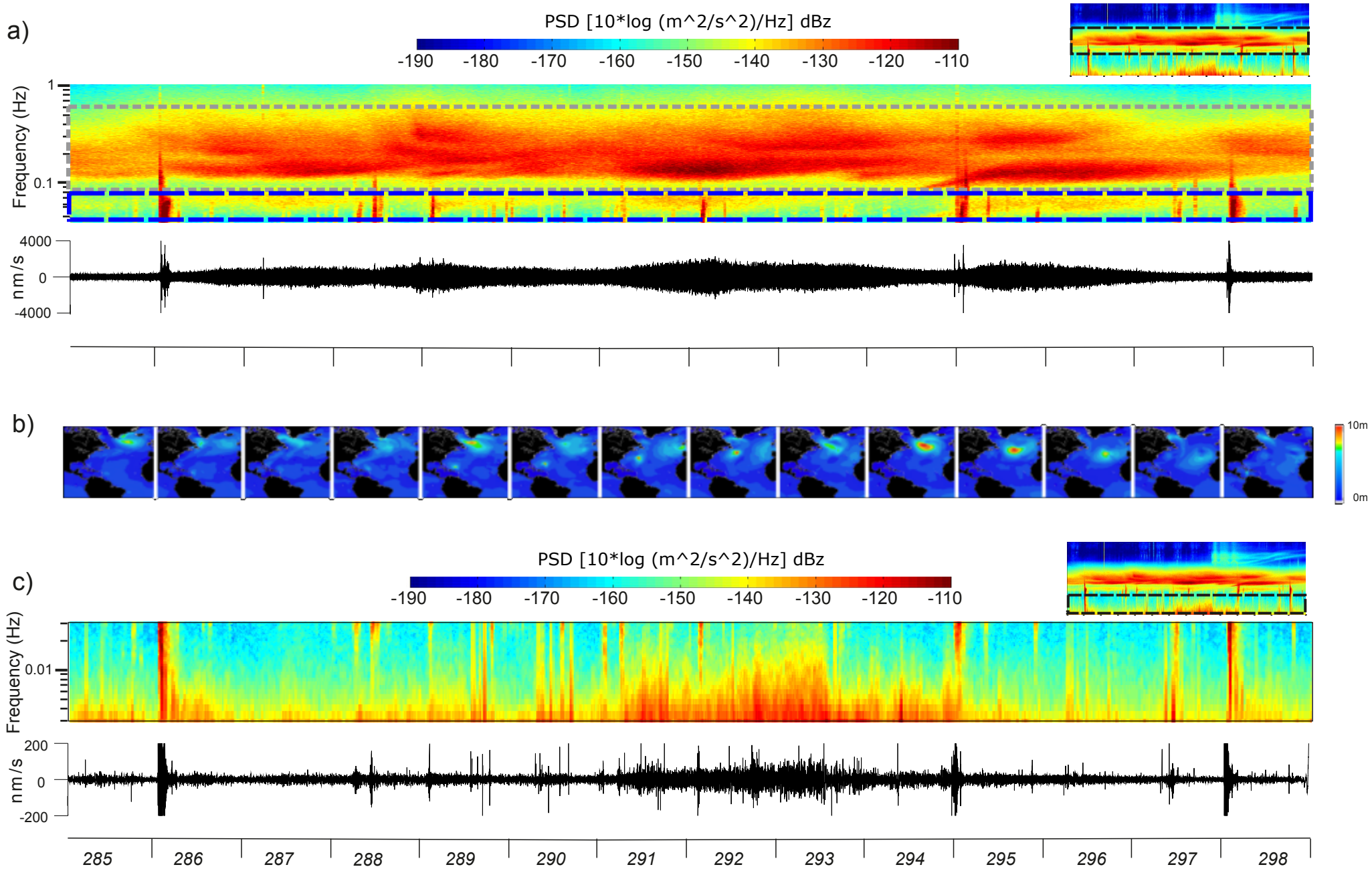

Figure 3: a) Upper panel: Spectrogram of the frequency range including the microseismic peak. The blue and grey dashed boxes outline respectively the primary and secondary microseismic peaks. Lower panel: seismic trace filtered between 0.04 and 0.8 Hz. b) Significant wave heighs from the Wavewatch III hindcast model. Each frame represents the snapshot at 12:00 of the corresponding day. c) Upper panel: Spectrogram for the earth's hum frequency range. Lower panel: Seismic trace bandpass filtered between 3 and 30 mHz. The insets allow to locate the analized intervals in the complete spectrogram.

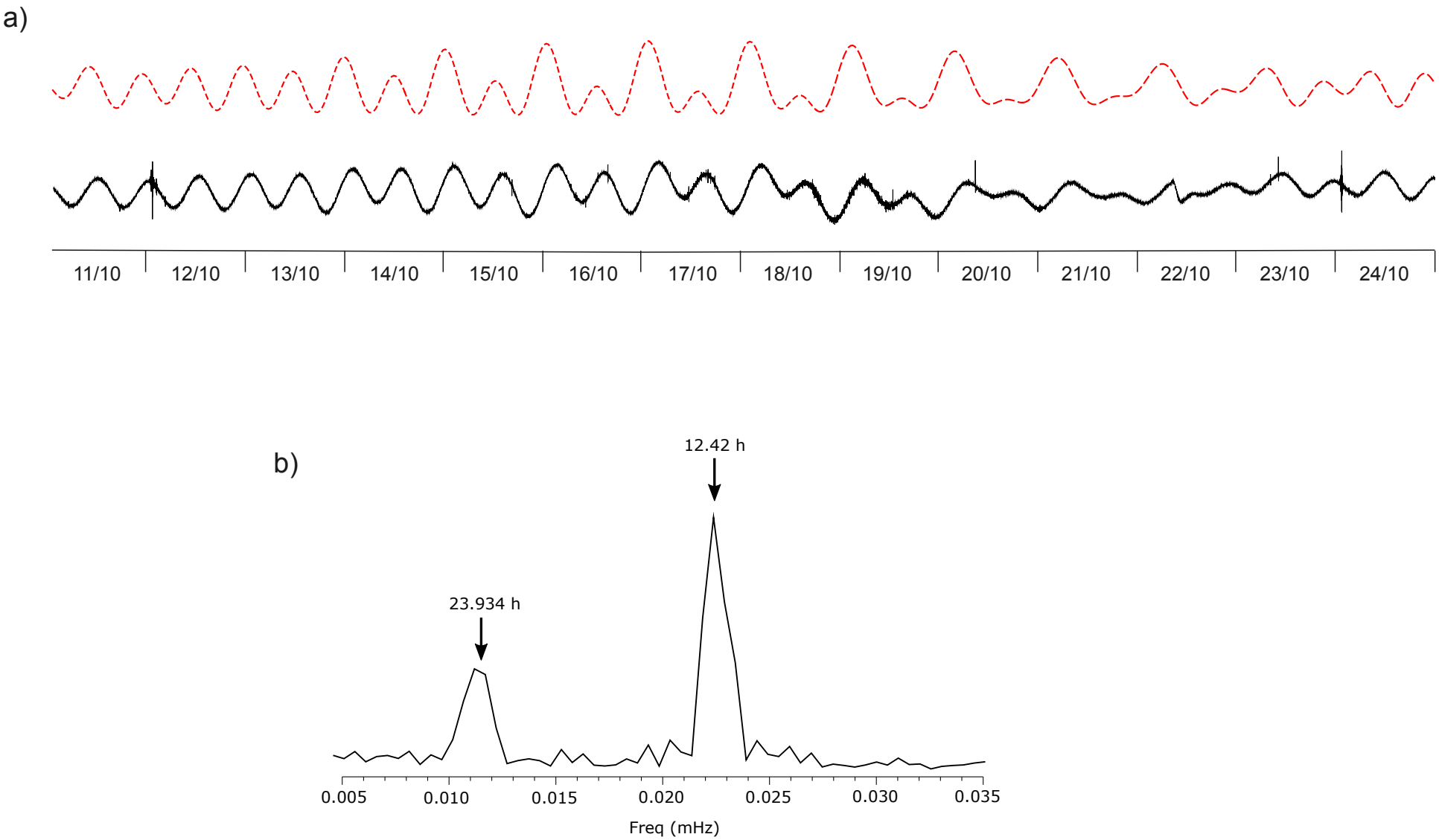

Figure 4: a) Theoretical solid Earth tide, represented as potential height (red dashed line) and raw vertical seismic trace downsampled to 1 sample per minute (black line). The correlation between both signals is clear for the semi-diurnal, diurnal and fortnightly components of tide. b) Spectrum of the seismic trace. The two peaks correspond to the frequencies of the main diurnal and semi diurnal components of tide, shown by arrows.

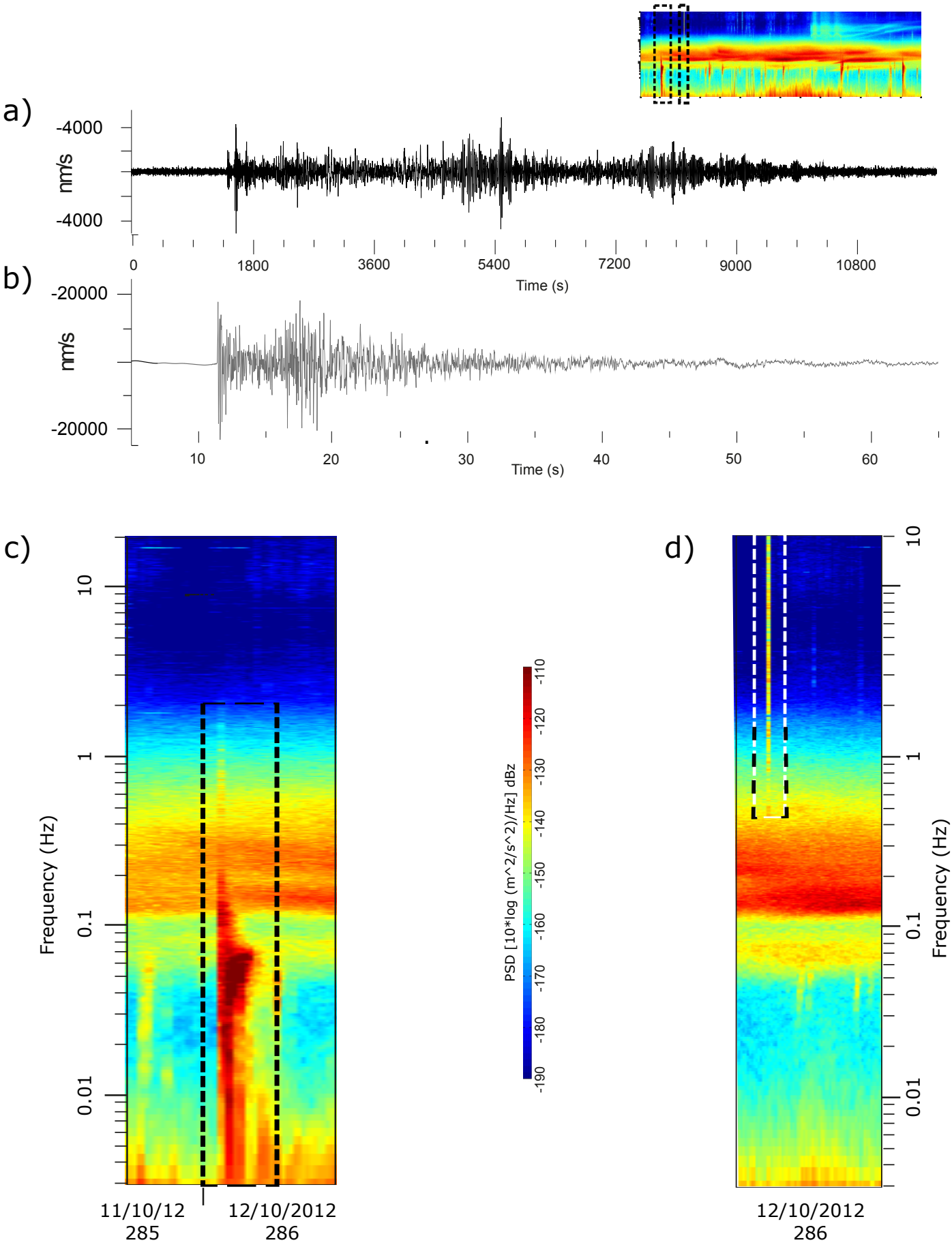

Figure 5: a,c) Seismic trace and corresponding spectrogram during the arrival of the seismic waves from a distant Mw 6.7 event with epicenter near the south coast of Papua, Indonesia (approx. distance: 14000 km). b,d) Seismic trace and corresponding spectrogram during the arrival of the seismic waves from a local event with magnitude 3.8 Mlv and epicenter near the town of Lourdes, approximately 60 km away from the recording site. Black boxes in the inset allow to locate both events.